Applied Physics Letters

RESEARCH ARTICLE | FEBRUARY 27 2026

Epitaxial growth and substitution control of SrIr$_{1-x}$Sn$_x$O$_3$ thin films by dual-beam pulsed laser deposition

Dapeng Cui ✉; Chengkun Xing; Anjila Ghimire; Dongliang Gong; Shashi Pandey; Lukas Horák;
Yan Xin; Haidong Zhou; Jian Liu ✉

Check for updates

Appl. Phys. Lett. 128, 082407 (2026)
https://doi.org/10.1063/5.0315770

CHORUS

View Online

Export Citation

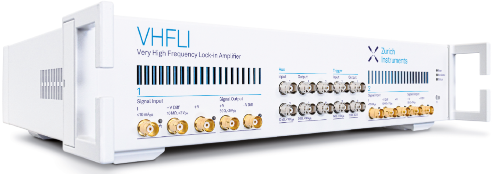

AIP Publishing

Epitaxial growth and substitution control of $SrIr_{1-x}Sn_xO_3$ thin films by dual-beam pulsed laser deposition

Cite as: Appl. Phys. Lett. **128**, 082407 (2026); doi: 10.1063/5.0315770
Submitted: 8 December 2025 · Accepted: 2 February 2026 ·
Published Online: 27 February 2026

Dapeng Cui,[1,a)] Chengkun Xing,[1] Anjila Ghimire,[1] Dongliang Gong,[1] Shashi Pandey,[1] Lukas Horák,[2] Yan Xin,[3] Haidong Zhou,[1] and Jian Liu[1,a)]

AFFILIATIONS

[1] Department of Physics and Astronomy, University of Tennessee, Knoxville, Tennessee 37996, USA
[2] Department of Condensed Matter Physics, Faculty of Mathematics and Physics, Charles University, Prague, 12116, Czech Republic
[3] National High Magnetic Field Laboratory, Florida State University, Tallahassee, Florida 32310, USA

[a)] **Authors to whom correspondence should be addressed:** dcui1@utk.edu and Jianliu@utk.edu

ABSTRACT

The emergent antiferromagnetic insulating phase of $SrIr_{1-x}Sn_xO_3$ has functional spintronic properties but is critically sensitive to the substitution concentration x, which is difficult to precisely tune in thin films grown by conventional pulsed laser deposition (PLD). We demonstrate the efficient composition control of epitaxial $SrIr_{1-x}Sn_xO_3$ thin films on $SrTiO_3(001)$ using a dual-beam PLD technique, co-ablating $SrIrO_3$ and $SrSnO_3$ targets. By controlling the relative beam intensity, we achieve wide-range tuning of x (from ~ 0.15 to ~ 0.45), which is estimated from using the out-of-plane lattice parameter c. This substitution control is confirmed by a systematic evolution of the magnetic and transport properties, including a monotonic increase in resistivity and a dome-like evolution of the Néel temperature and remnant magnetization. This work establishes dual-beam PLD as an efficient method for substitution control in iridates with the lattice parameter as a reliable indicator of the property evolution.

Pulsed laser deposition (PLD) is a mainstay for synthesizing complex oxide thin films because it exploits a highly non-equilibrium growth mode to transfer materials from a solid target to the substrate, given certain thermodynamic parameters and growth conditions.[1,2] It also has advantages in accommodating elements with high volatility and high melting point, and enabling rapid exploration of growth windows by adjusting substrate temperature, oxygen partial pressure, laser fluence, repetition rate, etc.[3,4] When coupled with *in situ* monitoring, atomic level control can be achieved to create epitaxial heterostructures of complex oxides,[5,6] providing a platform to study interfacial coupling and emergent properties.[7–12] A practical limitation, however, arises when tuning the stoichiometry for doping or substitution control. Not only are different targets needed for different compositions within a substitution series but also the fabrication or preparation of the targets must ensure they have the same density, purity, microstructure, etc. Otherwise, the film's consistency will be impacted. Although the film stoichiometry does depend to some extent on the parameters mentioned above,[1,3–5] i.e., temperature, pressure, fluence, and so on, their influence on composition is indirect because they either do not change the mass ratio of the different plasma species or change it while significantly changing the plume dynamics.[4,13] This is in contrast to molecular beam epitaxy, which provides truly independent sources of different elements with real time flux control,[14,15] and magnetron sputtering, where co-sputtering from multiple targets can effectively tune the film composition.[16,17]

Efforts in addressing the challenge of PLD in composition exploration and control have focused on combinatorial PLD, which sequentially ablates different targets to alternatively deposit submonolayers. This can be achieved by sequential pulsing between different targets with programmed pulse ratios.[18] Another approach is to use a motor-driven shadow mask, resulting in a lateral composition spread upon solid state diffusion of the different target materials.[5,19–22] However, the diffusivity on the substrate surface could be a limitation.[20,23] Macroscopic property measurements and device fabrication would still require homogeneous samples.[5,19] An alternative method is dual-beam PLD, where two targets are ablated simultaneously, intermixing the species before their arrival on the substrate surface as a co-deposition technique.[24,25] It can produce a tunable homogeneous composition with a small beam spot separation, as well as a composition gradient with a large separation.[26,27] This technique was in fact demonstrated before combinatorial PLD but has been studied much less despite its versatility and lower cost. $SrIr_{1-x}Sn_xO_3$ is a representative material[28,29] that could benefit from dual-beam PLD. Its parent phase, perovskite $SrIrO_3$, is a nonmagnetic topological semimetal in proximity to an antiferromagnetic insulating phase due to electron correlation.[30–33] Interestingly, this Mott transition can be triggered by isovalent substitution of Ir^{4+} ions with nonmagnetic Sn^{4+} ions at low concentrations.[28,34] Although the exact mechanism remains unknown, the antiferromagnetic ordering temperature T_N increases rapidly with x and reaches its maximum at $x = 0.2$.[28] Unfortunately, bulk crystals are limited to polycrystalline samples due to high-pressure synthesis.[28,29] Epitaxial growth by PLD has offered a great solution to obtain single crystalline samples,[34,35] enabling the observation of the anomalous Hall effect and anomalous Nernst effect within the antiferromagnetic insulating phase.[36] However, reported film growth has been limited to single-beam PLD. Only one study attempted to synthesize films of different substitution concentrations using separate targets.[34]

In this work, we demonstrated dual-beam PLD growth of epitaxial $SrIr_{1-x}Sn_xO_3$ (SIO_Sn) thin films. Our results show that, by controlling the relative laser-beam fluence delivered to the two targets, we were able to achieve a fine compositional tuning around $x = 0.2$ and extend the covered range well beyond that. The substitution control is evidenced by both magnetization and resistivity measurements, which display a strong correlation and a systematic evolution as a function of the out-of-plane lattice parameter c. Dual-beam PLD thus provides a practical and flexible route to study the rich correlation-topology interplay in SIO_Sn.

The SIO_Sn films were deposited on (001)-oriented $SrTiO_3$ (STO) substrates by simultaneously ablating $SrIrO_3$ (SIO) and $SrSnO_3$ (SSO) ceramic targets with a 248 nm KrF excimer laser at a repetition of 4 Hz. The STO substrates were TiO_2-terminated by standard buffered-HF-based treatment, including etching for 60 s followed by air annealing at 1050 °C for 120 min. The schematic diagram of the dual-beam PLD setup is shown in Fig. 1. The original beam is split by a beam splitter into two beams, "beam 0" (B0) and "beam 1" (B1), which are further focused on the targets separately. The diameter of both targets is 1 in. (25.4 mm). They rotate and wiggle simultaneously at the same speed using a standard spinning target carousel during the deposition. To maximize plume overlap while still allowing the wiggling motion, the beam spots on the two targets are separated by 16 mm, which is small enough for the growth to be considered in the homogeneous composition regime.[24,25] At this geometry, the substrate is positioned 55 mm from the targets at the plume center of B0. B0 was used to ablate the SIO target, and its beam spot is aligned to the substrate since SIO is the parent phase. Meanwhile, B1 was used to ablate the SSO target to introduce substitution. The path of B1 can host a high optical density attenuator to achieve coarse control (if needed) of the intensity relative to B0 and 8 ultraviolet (UV)-grade fused silica attenuators to fine-tune the energy ratio of the two beams, with each attenuator decreasing the intensity of B1 by ~10%. To increase Sn substitution, the growth was carried out by decreasing the number N of these B1 attenuators, while the laser fluence of B0 for the SIO target was fixed at 2.4 J/cm^2.

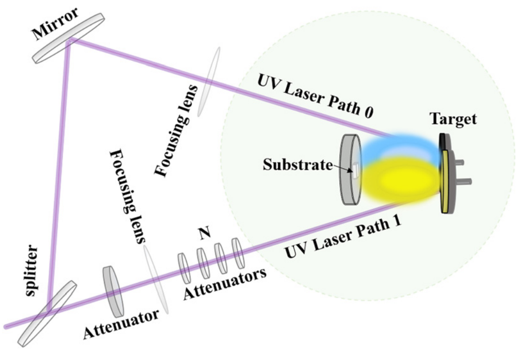

FIG. 1. Schematic of the dual-beam PLD configuration. A beam splitter generates two UV laser paths that are routed to the deposition chamber via relay optics. Path 0 delivers a fixed pulse energy to the target, whereas path 1 passes through a calibrated stack of optical attenuators to adjust its pulse energy and hence the energy density at the target. *N* denotes the number of attenuators inserted in path 1 after the focusing lens. By directing path 0 and path 1 to the SIO and SSO targets, respectively, the relative ablation fluxes are set *in situ*, enabling continuous control of the Sn incorporation *x* during epitaxial growth of SIO_Sn on a heated substrate. The colored plume (yellow/blue) illustrates the expanding plasma produced by laser ablation.

The substrate temperature and oxygen pressure were kept at 700 °C and 0.1 mbar in the chamber, respectively. The same number of pulses was given for each sample. Structure analysis was performed using a Panalytical X'Pert MRD diffractometer with an x-ray wavelength of 1.5406 Å using a Cu Kα radiation. Temperature dependent resistivity of the SIO_Sn films was measured by the four-terminal configuration with an in-line geometry from 5 to 300 K using a physical property measurement system (PPMS) from Quantum Design. Magnetization measurements were carried out on the vibrating sample magnetometer (MPMS3-VSM) from Quantum Design. The cross-sectional scanning transmission electron microscopy (STEM) with energy-dispersive x-ray spectroscopy (EDS) was conducted using a cold field emission probe-aberration-corrected JEOL JEMARM200cF at 200 kV.

For $SrIr_{1-x}Sn_xO_3$, the substitution concentration x is known to closely correlate with the lattice parameter,[28,29] which in the pseudocubic cell increases by ~0.010 Å for every 0.1 of x. The larger x is, the larger the lattice parameter is, following Vegard's law. For thin films grown on STO with a nominal value of $x = 0.2$, the out-of-plane lattice parameter c has been shown to be around 4.028 Å.[35] To bring the coarse control to the vicinity of this value, we first performed calibration growth and found that a 45 % coarse attenuation together with $N = 8$ resulted in c around 4.014 Å, giving rise to an appropriate starting point to systematically increase the lattice parameter by decreasing N to demonstrate substitution control around $x = 0.2$. We have reduced N down to 2. All samples were found to be single-phase by x-ray diffraction (XRD). Figure 2(a) is a representative $\theta - 2\theta$ XRD scan, which shows the phase purity even at a high substitution level expected for $N = 2$. Figure 2(b) shows scans around the STO (002) peak. A clear epitaxial film peak of the perovskite phase can be seen on the left, and its position indeed systematically shifts to lower angles with respect to a reference $x = 0$ sample when decreasing N, indicative of an increasing c. At $N = 5$, c is already above 4.035 Å [Fig. 2(c)]. It shows a relatively larger increase from $N = 5$ to 4. When N dropped

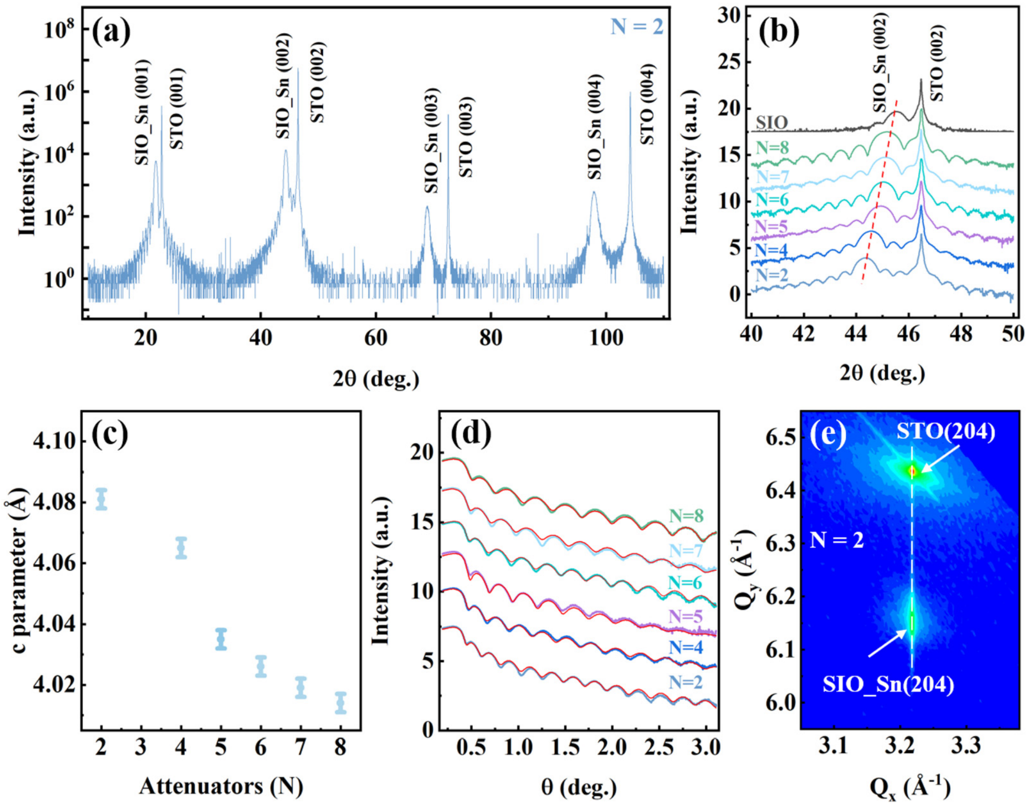

FIG. 2. Structural characterization of SIO_Sn thin films grown on the STO(001) substrate deposited at various attenuators under an oxygen partial pressure of 0.1 mbar at 700 °C. (a) XRD $\theta - 2\theta$ scan around the (00*l*) peak of the SIO_Sn film under $N = 2$. (b) XRD $\theta - 2\theta$ scans around the (002) peak of the SIO_Sn films. (c) Summary of the lattice parameter of *c*, which is extracted from figure (b), error bars denote fitting uncertainties. (d) XRR of the SIO_Sn films. XRR was measured in a symmetric $\theta - 2\theta$ specular geometry and plotted as a function of the incident angle θ. The red curves are fitting that extracts the thickness. (e) RSM of the $N = 2$, which is around the (204) diffraction peak of the STO substrate, showing the SIO_Sn (204) diffraction peak in pseudocubic notation, which demonstrates a fully strained state. The upper and lower peaks correspond to the STO and SIO_Sn (204) reflections, respectively. The white dashed line indicates the fully strained condition for the films where they were supposed to be located.

to 2, it increased to ∼4.081 Å, which is well above the target range and is indicative of a large *x*. The presence of Laue oscillations is also consistent with the epitaxial growth.

Figure 2(d) shows the x-ray reflectivity (XRR) from the SIO_Sn films. The thickness fringes indicate a well-defined SIO_Sn/STO interface and reasonably smooth surface/interfaces. The film thickness was fitted using a standard reflectivity model, which increases with decreasing *N* and ranges from ∼13 to ∼18 nm (see supplementary material Table S1). This is consistent with the fact that the SSO ablation was more intense with a higher B1 intensity. Since the cubic STO substrate has a lattice parameter $a = 3.905$ Å, using pseudocubic parameters $a_{\mathrm{pc}}(\mathrm{SIO}) \approx 3.950$ Å and $a_{\mathrm{pc}}(\mathrm{SSO}) \approx 4.036$ Å,[37,38] the in-plane misfit to STO(001) is −1.2% and −3.4%, respectively, corroborating the compressive-strain condition across the series. The SIO_Sn films are subject to an in-plane compressive strain due to the lattice mismatch that increases with increasing *x*. X-ray reciprocal space mapping (RSM) revealed that the SIO_Sn films are fully strained to the STO substrates (see supplementary material Fig. S1; for additional $\theta - 2\theta$ scans, see Fig. S2). A representative mapping around the (204) peak of the STO substrate in Fig. 2(e) shows that even the highest-substitution sample, i.e., $N = 2$, is still fully strained. This observation is also consistent with the fact that *c* of the SIO_Sn films is larger than the bulk value. For reference, we also deposited an SSO film on STO which has a relaxed bulk-like *c*-axis lattice parameter, consistent with prior reports that SSO tends to relax on STO due to the large mismatch[38–40] (see supplementary material Fig. S3).

The substitution control indicated by the close correlation between *c* and *N* is also well captured by the magnetic and electronic properties of the films. For comparison, an undoped SIO thin film grown under identical conditions is included in Figs. 3(a) and 3(b). As shown in Fig. 3(a), the in-plane remnant magnetization displays a systematic evolution with *N*. Specifically, the SIO_Sn film grown with $N = 8$ shows a weak ferromagnetic transition around 143 K, which signals the transition to the canted G-type antiferromagnetic order of the Ir $J_{\mathrm{eff}} = 1/2$ moments.[28,35] The transition temperature increases up to ∼225 K upon decreasing *N* to 5 and the remnant magnetization increases at the same time. This behavior is consistent with the increase in substitution as reported for the bulk.[28,29] A further reduction of *N* decreases the transition slightly to 200 K, and the remnant magnetization decreases as well. In contrast, the transition temperature was shown to remain the same in the bulk polycrystalline samples when $x = 0.2$ and above.[28] The observed magnetic evolution

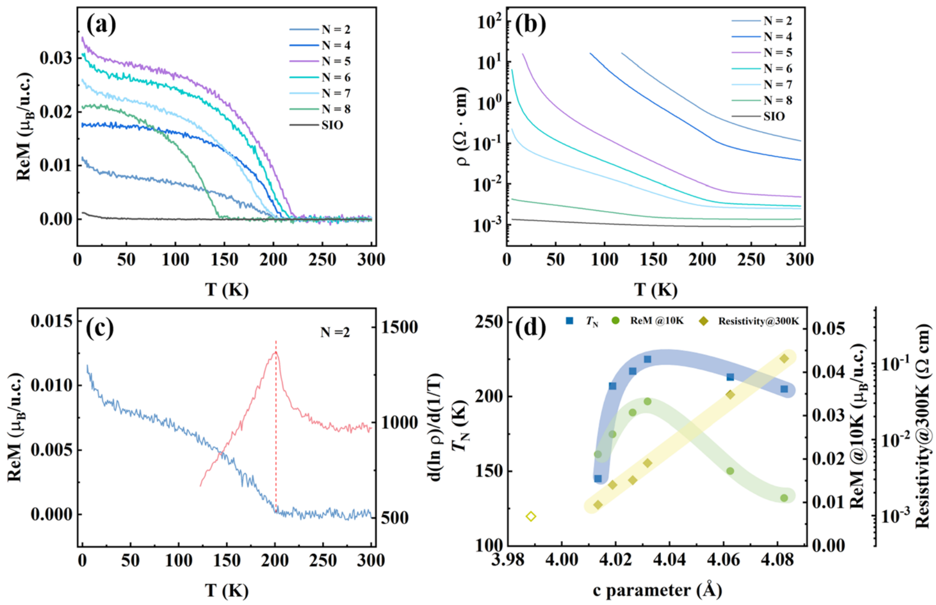

FIG. 3. (a) and (b) are the temperature dependence of remnant moment per unit cell (ReM) within the *ab*-plane and resistivity ($\rho - T$) curves of the SIO_Sn films grown with different attenuator numbers *N* in Path 1, respectively. An undoped SIO film ($x = 0$) grown under identical conditions is included for comparison. (c) Representative determination of the Néel transition temperature (T_N) for $N = 2$, the temperature dependence of $d\ln\rho/d(1/T)$ (right axis), which coincides with the transition in ReM(*T*) (left axis). The red vertical dashed line represents T_N, furnishing a consistent criterion used throughout this work. (d) Summary of key observables vs the out-of-plane lattice parameter *c*, T_N (left axis, blue squares), magnetization ReM of 10 K (right axis, green circles), and room temperature resistivity ρ(300 K) (right axis, yellow diamonds). T_N and ReM exhibit a dome-like evolution with *c*, while ρ(300 K) increases monotonically. For comparison, the room temperature resistivity of the SIO thin film is represented by an open yellow diamond.

is summarized in Fig. 3(d) as a function of the *c* parameter. Similar to previous studies on SIO_Sn films on STO(001),[34,35] the transition temperature is noticeably lower than the bulk,[28] which is likely due to the compressive-strain effect that increases the bandwidth of the $J_{\text{eff}} = 1/2$ electrons and reduces the magnetic instability.[41]

The corresponding evolution in temperature-dependent resistivity is shown in Fig. 3(b). All samples show insulating behavior, but to different extents. Specifically, resistivity increases with decreasing *N*, and the sample also becomes more insulating. The $N = 8$ sample is only weakly insulating, since the increase in resistivity down to 5 K remains within the same order and the sample remains relatively conductive at base temperature, indicative of a relatively light substitution. After lowering *N* down to 2, the resistivity at 300 K is two orders higher, and it rapidly increases upon cooling and exceeds the measurement limit at ∼125 K, consistent with a high concentration of Sn substitution.[28,29,34] Figure 3(d) summarizes the systematic resistivity increase as a function of *c* at 300 K in the logarithmic scale. In addition, a kink can be observed for each sample around the magnetic transition, where the increase in resistivity accelerates upon cooling. This can be better seen by taking the derivative $d\ln\rho/d(1/T)$. Figure 3(c) shows an example, where a λ-like cusp peak of the derivative can be clearly seen near the onset temperature of the remnant magnetization, consistent with a strong coupling between electronic properties and magnetic ordering in SIO_Sn.[28,34]

The systematic evolution of both magnetic and electronic properties shown in Fig. 3(d) confirms that the lattice parameter serves as a practical *in situ* empirical proxy for *x* under our compressive-strain conditions for the substitution control by dual-beam deposition. However, because of the compressive strain, the out-of-plane lattice parameters cannot be directly compared with the bulk ones. To calibrate the substitution concentration of the films, we measured EDS on a $N = 5$ sample by cross-sectional TEM. Figure 4(a) shows the cross-sectional high-angle annular dark-field scanning transmission electron microscopy (HAADF-STEM) image viewed along [100] of STO, where a sharp epitaxial interface can be seen. The cross-sectional STEM-EDS elemental maps in Figs. 4(c)–4(e) confirm no significant interdiffusion across the film/substrate interface. The measured Ir:Sn ratio is about 1:0.304(25), corresponding to a substitution concentration $x = 0.233(15)$. Meanwhile, the ratio between the A- and B-site cations is close to unity, with Sr/(Ir+Sn)=1.004(2), indicating a near-stoichiometric composition. By using *c* at $N = 5$ for $x = 0.233$ and *c* of the reference SIO sample for $x = 0$, one can infer the substitution concentration of all samples, which is plotted against *c* in Fig. 4(b) by assuming Vegard's law remains valid. One can see that a wide range of *x* was covered by the samples. The $N = 8$ sample has an *x* close to 0.15, which is consistent with its lower transition temperature and low resistivity as well as the expectation from the coarse intensity control of B1, which was to set a starting point for *x* slightly below 0.2. Meanwhile, the $N = 2$ sample with *c* greater than 4.081 Å has a large *x* around 0.45, consistent with high resistivity and small magnetization. The substitution concentrations of the samples together with their magnetic and electronic evolution again demonstrate that *c* provides a practical estimation of the property tuning and the underlying change in *x* for our SIO_Sn series on STO. We also did another analysis by including the impact of strain via the Poisson's ratio. The result shows that the $c - x$ relation in that case deviates from the linear relation of

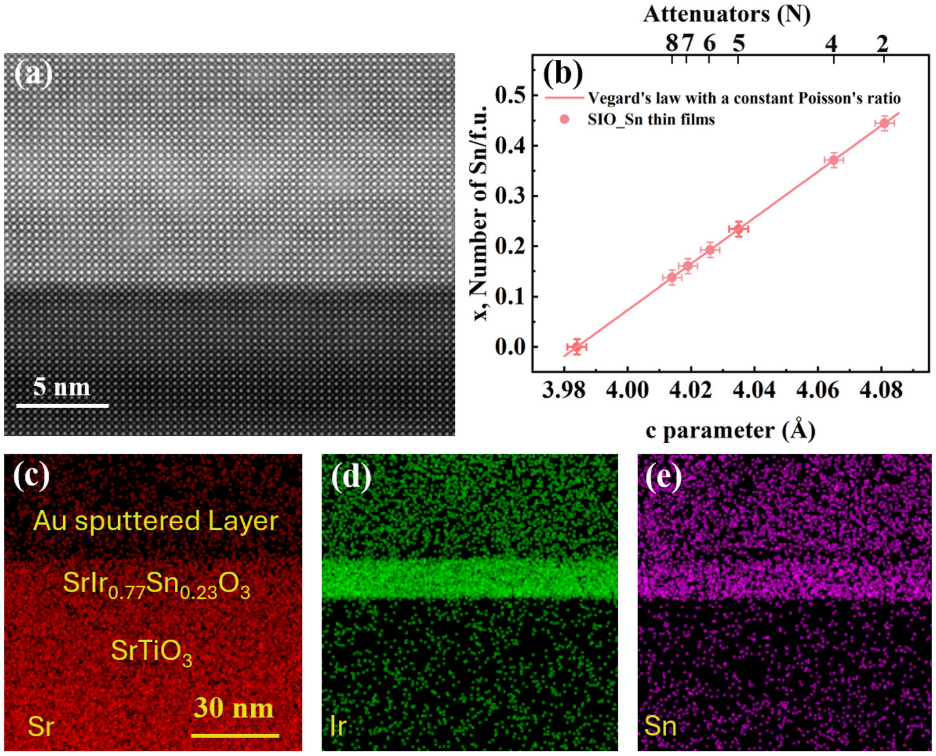

FIG. 4. (a) Cross section HAADF-STEM image of SIO_Sn thin film growth on STO(001) substrate along the [100] projection for $N = 5$. The corresponding elemental compositions were extracted via EDS. (b) Empirical correlation between the out-of-plane lattice parameter c and the inferred Sn content x for the SIO_Sn films under various number of attenuators. Calibration of x vs c anchored by two points, $x = 0$ for the undoped SIO and $x = 0.233(15)$ for the $N = 5$ film from EDS results, which points display darker in the figure. The solid red line is used to estimate x from c throughout the study, consistent with the monotonic increase in c with Sn incorporation. The top axis labels the discrete attenuator number N for each sample. EDS images of the SIO_Sn film for $N = 5$. (c) Sr EDS map; (d) Ir EDS map; (e) Sn EDS map. The EDS results demonstrate that there is no significant interdiffusion across the interface.

Vegard's law, but the difference at small x is within the measurement uncertainties (see supplementary material Fig. S4).

The results clearly show that dual-beam PLD affords an efficient co-deposition method for substitution tuning in epitaxial SIO_Sn thin films, since one only needs two targets. In contrast, previous studies by conventional single-beam PLD relied on multiple composition-specific targets. Although one no longer has a nominal substitution concentration in dual-beam PLD, our results indicate that the lattice parameter of the resulting films is the control parameter for the purpose of tuning the magnetic and electronic properties. In addition, dual-beam PLD may easily incorporate many other beam parameters to further control the substitution, such as beam spot separation, beam focusing, substrate position, etc. Each could engage a different aspect of the dynamics of the two plumes, opening a multi-dimensional phase space of the composition control.

In summary, we have demonstrated that dual-beam PLD is a highly effective and efficient method for controlling the substitution concentration x in epitaxial SIO_Sn thin films. By co-ablating SIO and SSO targets and adjusting the relative beam intensity, we were able to bypass the need for multiple, costly composition-specific targets. In the absence of a nominal composition, the results show a systematic evolution of the electronic and magnetic properties with a clear correlation with c. Cross-sectional STEM-EDS analysis confirms negligible interdiffusion and near-stoichiometric Sr/(Ir+Sn). It provides a practical and cost-effective approach for fine and continuous composition tuning in this dual-beam PLD geometry. For future directions, it would be interesting to tune the intensities of both beams for investigating the complete fluence dependence as well as systematically compare the composition control with other PLD techniques.

See the supplementary material for a compilation of additional characterization that supports the main text. (i) Table S1, the fitting results of SIO_Sn films grown with different attenuators. (ii) Figure S1, RSMs near the STO(204) reflection for SIO_Sn films deposited on STO(001) under an oxygen partial pressure of 0.1 mbar at 700 °C for $N = 4$–8. (iii) Figure S2, $\theta - 2\theta$ scans around the (00l) reflection for SIO_Sn films deposited on STO(001) under an oxygen partial pressure of 0.1 mbar at 700 °C for $N = 4$–8. (iv) Figure S3, summary of the structure and magnetic characterization of SSO thin film grown on STO under the same conditions. (v) Figure S4, comparison between the empirical c–x calibration and a Poisson-ratio-based elastic estimate.

The design and assembly of the dual-beam setup were supported by the U.S. Department of Energy under Grant No. DE-SC0020254. Materials synthesis and characterization were supported by the National Science Foundation under Grant No. DMR-1848269. C.X. and S.P. acknowledge the Graduate Support Program from the Center for Material Processing at the University of Tennessee, Knoxville. Part of the work was done in the National High Magnetic Field Laboratory, which is supported by the National Science Foundation Cooperative Agreement No. DMR-2128556 and the State of Florida.

AUTHOR DECLARATIONS

Conflict of Interest

The authors have no conflicts to disclose.

Author Contributions

Dapeng Cui: Conceptualization (equal); Data curation (equal); Formal analysis (equal); Investigation (equal); Methodology (equal); Project administration (equal); Resources (equal); Software (equal); Validation (equal); Visualization (equal); Writing – original draft (equal); Writing – review & editing (equal). **Chengkun Xing:** Conceptualization (equal); Data curation (supporting); Formal analysis (supporting); Investigation (equal); Methodology (equal); Software (equal); Writing – original draft (supporting); Writing – review & editing (supporting). **Anjila Ghimire:** Investigation (supporting); Methodology (supporting). **Dongliang Gong:** Data curation (supporting); Formal analysis (supporting); Investigation (supporting); Methodology (supporting); Writing – original draft (supporting); Writing – review & editing (supporting). **Shashi Pandey:** Investigation (supporting); Methodology (supporting). **Lukas Horák:** Data curation (lead); Formal analysis (equal); Software (equal). **Yan Xin:** Data curation (lead); Formal analysis (equal); Software (equal). **Haidong Zhou:** Data curation (supporting); Funding acquisition (lead); Project administration (equal); Supervision (equal); Writing – original draft (supporting); Writing – review & editing (supporting). **Jian Liu:** Conceptualization (equal); Data curation (equal); Formal analysis (equal); Funding acquisition (equal); Investigation (equal); Methodology (equal); Project administration (equal); Resources (equal); Software (equal); Supervision (equal); Validation (equal); Visualization (equal); Writing – original draft (equal); Writing – review & editing (equal).

DATA AVAILABILITY

The data that support the findings of this study are available from the corresponding authors upon reasonable request.

REFERENCES

[1] R. Eason, *Pulsed Laser Deposition of Thin Films: Applications-Led Growth of Functional Materials* (John Wiley & Sons, 2006).
[2] D. H. Blank, M. Dekkers, and G. Rijnders, J. Phys. D: Appl. Phys. **47**, 034006 (2014).
[3] P. Willmott and J. Huber, Rev. Mod. Phys. **72**, 315 (2000).
[4] N. A. Shepelin, Z. P. Tehrani, N. Ohannessian, C. W. Schneider, D. Pergolesi, and T. Lippert, Chem. Soc. Rev. **52**, 2294 (2023).
[5] H. M. Christen and G. Eres, J. Phys. Condens. Matter **20**, 264005 (2008).
[6] J. Boschker and T. Tybell, Appl. Phys. Lett. **100**, 151604 (2012).
[7] H. Y. Hwang, Y. Iwasa, M. Kawasaki, B. Keimer, N. Nagaosa, and Y. Tokura, Nat. Mater. **11**, 103 (2012).
[8] J. Chakhalian, J. W. Freeland, A. J. Millis, C. Panagopoulos, and J. M. Rondinelli, Rev. Mod. Phys. **86**, 1189 (2014).
[9] H. Jang, D. Felker, C. Bark, Y. Wang, M. K. Niranjan, C. Nelson, Y. Zhang, D. Su, C. Folkman, S. Baek *et al.*, Science **331**, 886 (2011).
[10] C. Ahn, A. Cavalleri, A. Georges, S. Ismail-Beigi, A. J. Millis, and J.-M. Triscone, Nat. Mater. **20**, 1462 (2021).
[11] R. Ramesh and D. G. Schlom, Nat. Rev. Mater. **4**, 257 (2019).
[12] S. Das, A. Ghosh, M. R. McCarter, S.-L. Hsu, Y.-L. Tang, A. R. Damodaran, R. Ramesh, and L. W. Martin, APL Mater. **6**, 100901 (2018).
[13] A. Ojeda-G-P, M. Döbeli, and T. Lippert, Adv. Mater. Interfaces **5**, 1701062 (2018).
[14] D. G. Schlom, APL Mater. **3**, 062403 (2015).
[15] W. Nunn, T. K. Truttmann, and B. Jalan, J. Mater. Res. **36**, 4846 (2021).
[16] P. J. Kelly and R. D. Arnell, Vacuum **56**, 159 (2000).
[17] J. Anguita, M. Thwaites, B. Holton, P. Hockley, and S. Rand, J. Vac. Sci. Technol. A **23**, 265 (2005).
[18] K. A. Stoerzinger, L. Wang, Y. Ye, M. Bowden, E. J. Crumlin, Y. Du, and S. A. Chambers, J. Mater. Chem. A **6**, 22170 (2018).
[19] N. Bassim, P. K. Schenck, M. Otani, and H. Oguchi, Rev. Sci. Instrum. **78**, 072203 (2007).
[20] H. Christen, S. Silliman, and K. Harshavardhan, Rev. Sci. Instrum. **72**, 2673 (2001).
[21] K. Chang, M. Aronova, O. Famodu, I. Takeuchi, S. Lofland, J. Hattrick-Simpers, and H. Chang, Appl. Phys. Lett. **79**, 4411 (2001).
[22] H. Koinuma and I. Takeuchi, Nat. Mater. **3**, 429 (2004).
[23] A. Venimadhav, K. Yates, and M. Blamire, J. Comb. Chem. **7**, 85 (2005).
[24] A. Ito, A. Machida, and M. Obara, Appl. Phys. Lett. **70**, 3338 (1997).
[25] R. W. Eason, T. C. May-Smith, K. A. Sloyan, R. Gazia, M. S. B. Darby, A. Sposito, and T. L. Parsonage, J. Phys. D: Appl. Phys. **47**, 034007 (2014).
[26] J. Sakai, J. M. C. Roque, P. Vales-Castro, J. Padilla-Pantoja, G. Sauthier, G. Catalan, and J. Santiso, Coatings **10**, 540 (2020).
[27] B. Hussey and A. Gupta, J. Appl. Phys. **72**, 287 (1992).
[28] Q. Cui, J.-G. Cheng, W. Fan, A. E. Taylor, S. Calder, M. A. McGuire, J.-Q. Yan, D. Meyers, X. Li, Y. Cai *et al.*, Phys. Rev. Lett. **117**, 176603 (2016).
[29] J. Fujioka, T. Okawa, M. Masuko, A. Yamamoto, and Y. Tokura, J. Phys. Soc. Jpn. **87**, 123706 (2018).
[30] Y. F. Nie, P. King, C. Kim, M. Uchida, H. Wei, B. D. Faeth, J. Ruf, J. Ruff, L. Xie, X. Pan *et al.*, Phys. Rev. Lett. **114**, 016401 (2015).
[31] S. Moon, H. Jin, K. W. Kim, W. Choi, Y. Lee, J. Yu, G. Cao, A. Sumi, H. Funakubo, C. Bernhard *et al.*, Phys. Rev. Lett. **101**, 226402 (2008).
[32] M. A. Zeb and H.-Y. Kee, Phys. Rev. B **86**, 085149 (2012).
[33] J.-M. Carter, V. V. Shankar, M. A. Zeb, and H.-Y. Kee, Phys. Rev. B **85**, 115105 (2012).
[34] M. Negishi, N. Hiraoka, D. Nishio-Hamane, and H. Takagi, APL Mater. **7**, 121101 (2019).
[35] J. Yang, L. Hao, Q. Cui, J. Lin, L. Horak, X. Liu, L. Zhang, H. Yang, J. Karapetrova, J.-W. Kim *et al.*, Phys. Rev. Mater. **3**, 124411 (2019).
[36] D. Gong, J. Yang, S. Zhang, S. Pandey, D. Cui, J. P. Ruff, L. Horak, E. Karapetrova, J.-W. Kim, P. J. Ryan *et al.*, Nat. Commun. **16**, 2888 (2025).
[37] T. Anderson, S. Ryu, H. Zhou, L. Xie, J. Podkaminer, Y. Ma, J. Irwin, X. Pan, M. Rzchowski, and C. Eom, Appl. Phys. Lett. **108**, 151604 (2016).
[38] P.-Y. Chen, C. H. Lam, B. Edmondson, A. B. Posadas, A. A. Demkov, and J. G. Ekerdt, J. Vac. Sci. Technol. A **37**, 050902 (2019).
[39] G. Prathiba, S. Venkatesh, and N. H. Kumar, Solid State Commun. **150**, 1436 (2010).
[40] T. Wang, A. Prakash, Y. Dong, T. Truttmann, A. Bucsek, R. James, D. D. Fong, J.-W. Kim, P. J. Ryan, H. Zhou *et al.*, ACS Appl. Mater. Interfaces **10**, 43802 (2018).
[41] J. Yang, L. Hao, D. Meyers, T. Dasa, L. Xu, L. Horak, P. Shafer, E. Arenholz, G. Fabbris, Y. Choi, D. Haskel, J. Karapetrova, J.-W. Kim, P. J. Ryan, H. Xu, C. D. Batista, M. P. M. Dean, and J. Liu, Phys. Rev. Lett. **124**, 177601 (2020).